Journal of Materials Chemistry A

From Au-rich Core/PtNi-rich Shell to Ni-rich Core/PtAu-rich Shell: an Effective Thermochemical Pathway to Nanoengineering Catalysts for Fuel Cells

Journal:	*Journal of Materials Chemistry A*
Manuscript ID	TA-ART-01-2018-000025.R1
Article Type:	Paper
Date Submitted by the Author:	02-Feb-2018

Complete List of Authors:	Lu, Aolin; State University of New York at Binghamton, Department of Chemistry; Xiamen University, Department of Materials Science and Engineering Wu, Zhipeng ; State University of New York at Binghamton, Department of Chemistry Chen, Bing Hui; Xiamen University, Chemical & Biochemical Engineering Peng, Dong-Liang; Xiamen University, Department of Materials Science and Engineering Yan, Shan; State University of New York at Binghamton, Department of Chemistry Shan, Shiyao; State University of New York at Binghamton, Department of Chemistry Skeete, Zakiya; State University of New York at Binghamton, Department of Chemistry Chang, Fangfang; State University of New York at Binghamton, Department of Chemistry Chen, Yuanzhi; Xiamen University, Department of Materials Science and Engineering Zheng, Hongfei; Xiamen University, Chemical & Biochemical Engineering Zeng, Deqian; Xiamen University, Chemical & Biochemical Engineering YANG, Lefu; Catalysis, Chemistry Sharma, Anju; Binghamton University Luo, Jin; State University of New York at Binghamton, Department of Chemistry Wang, Lichang; Southern Illinois University, Chemistry and Biochemistry Petkov, Valeri; CMU, Physics Zhong, Chuan-jian; State University of New York at, Department of Chemistry

From Au-rich Core/PtNi-rich Shell to Ni-rich Core/PtAu-rich Shell: an Effective Thermochemical Pathway to Nanoengineering Catalysts for Fuel Cells

Aolin Lu[a,b], Zhipeng Wu[b], Binghui Chen[a], Dong-Liang Peng[a], Shan Yan[b], Shiyao Shan[b], Zakiya Skeete[b], Fangfang Chang[b], Yuanzhi Chen[a], Hongfei Zheng[a], Deqian Zeng[a], Lefu Yang[a], Anju Sharma[b], Jin Luo[b], Lichang Wang[c], Valeri Petkov[d], and Chuan-Jian Zhong[b]*

a) Department of Chemical and Biochemical Engineering, College of Chemistry and Chemical Engineering; and Department of Materials Science and Engineering, College of Materials, Xiamen University, Xiamen 361005, China.
b) Department of Chemistry, State University of New York at Binghamton, Binghamton, NY 13902, USA.
c) Department of Chemistry and Biochemistry, Southern Illinois University, Carbondale, Illinois 62901, USA.
d) Department of Physics, Central Michigan University, Mt. Pleasant, Michigan 48859, USA.
(* - Corresponding author, email: cjzhong@binghamton.edu)

Abstract: A major challenge in the design of nanocatalysts containing noble metals is the ability to engineer the relative surface composition and structure so that the catalytic activity and stability can be enhanced with minimum use of the noble metals. We demonstrate here this ability by an effective thermochemical pathway to enable the structural evolution of fuel cell nanocatalysts from Au-rich core/PtNi-rich shell to Ni-rich core/PtAu-rich shell. The synthesis starts from introduction of a third low-cost transition metal (nickel) into AuPt nanoparticles through a facile one-pot synthesis followed by thermochemical and electrochemical treatment. By exploiting the surface free energy differences among Au, Pt and Ni, the as-synthesized Au-rich core/PtNi-rich shell structure is transformed to Ni-rich core/PtAu-rich shell structure, producing a significant multifunctional synergy in comparison with bimetallic PtAu nanoparticles. The surface enrichment of PtAu with slightly-segregated Au, along with shrinking of Pt-Pt distances, is shown to enhance the dehydrogenation of methanol and effectively remove the surface carbonaceous species. The surface Au atoms facilitate maneuvering of the electrons in the oxidation reactions, whereas the positively-charged PtAu rich surface through electrochemical treatment enhances the oxidation activity. The mass activity of the nanocatalysts is shown to maximize as a function of Ni doping. The result is further supported by computational analysis of the adsorption energy of methanol on the nanoclusters, revealing that the increased catalytic activity correlates well with the decreased adsorption energy. The findings demonstrate an unprecedented ability to reverse the core-shell structure of the as-synthesized nanocatalysts for electrocatalytic enhancement, which has significant implication for the design of noble metal containing nanocatalysts for fuel cells.

Keywords: Core-shell nanocatalysts, nickel-doped platinum-gold nanoparticles, composition tunability, electrocatalytic oxidation of methanol, and catalytic synergy.

Broader context:

Fuel cells such as direct methanol or ethanol fuel cells represents a highly-effective pathway to meet the increasing energy needs to power portable devices, since the liquid fuels feature high volumetric energy and can be obtained from abundant biomass sources. However, the requirement of high-level noble metals in the catalysts constitutes a major barrier to the fuel cell commercialization. One of the increasingly-attractive approaches to addressing this problem focuses on wet-chemical synthesis of nanocatalysts with noble and non-noble metals, which often results in core-shell nanostructures or mesoporous nanoframes with undesired noble and non-noble metal distributions across the nanocatalysts for catalytic enhancement. Herein, this work reports a highly-effective thermochemical pathway convert as-synthesized Au-rich core/PtNi-rich shell into Ni-rich core/PtAu-rich shell nanoparticles. The novelty of this approach exploits the surface free energy differences among Au, Pt and Ni towards the desired noble and non-noble metal distributions across the nanocatalysts for the catalytic enhancement, which serves as a new strategy for the preparation and optimization of active and stable binary/ternary nanoparticles for advancing catalyst design in fuel cell technology.

1. Introduction

Two of the major problems in the development of direct methanol oxidation fuel cells (DMFC) include poor activity of the anode catalysts and ‘‘methanol crossover” to the cathode electrode,[1, 2] which lead to a loss of about one-third of the available energy at the cathode and another one-third at the anode. For the anode reaction of DMFC, Pt is one of the most active catalysts, but it subjects to propensity of poisoning by CO-like intermediate species.[3-5] To address the problem, the design of bimetallic AuPt nanostructures has been a focal point of increasing research interests[6-8], which takes advantage of Au nanoparticles showing unprecedented catalytic activities for CO and methanol oxidation.[9-15] Moreover, alloying Pt with a second transition metal provides synergistic activities for the suppression of adsorbed poisonous species and the change of electronic band structure.[16-19] For methanol oxidation reaction (MOR), Pt serves as the main sites for dehydrogenation of methanol whereas Au provides surface-oxygenated species to favor the removal of them.[20-22] Au also functions as an electronic sink in promoting the oxidation reaction by exhausting negative charges.[23] Indeed, PtAu exhibits bifunctional synergy for electrocatalytic MOR in alkaline electrolytes,[24] and oxygen reduction reaction in acidic electrolyte.[25-26] However, PtAu show much lower activities for MOR in acidic electrolytes [22, 24] due to the suppression of surface-oxygenated species. The d band center of Pt has been considered to be shifted positively as a result of tensile strains by the expansion of Pt lattice in PtAu alloy (Au atom is larger than Pt atom), which however strengthens the adsorption of surface carbonaceous species.[16]

One of the major challenges in the design of nanocatalysts containing noble metals is the ability to engineer the relative surface composition and structure so that the catalytic activity and stability can be enhanced with minimum use of the noble metals. Here we demonstrate an effective thermochemical pathway to enable the structural evolution of nanocatalysts from as-synthesized Au-rich core/PtNi-rich shell to Ni-rich core/PtAu-rich shell nanostructures. The concept of the introduction of a third transition base metal into PtAu alloy stems from the consideration of lattice shrinking, d-band center lowering, and carbonaceous species adsorption

weakening for Pt upon alloying with many transition base metals.[16] Moreover, base transition metals exhibit oxyphilic character which would impact the surface partial charge characteristic for maneuvering the surface-oxygenated species. It is thus hypothesized that the introduction of Ni into AuPt alloy could produce synergistic properties in terms of the interatomic distances, the partial surface charges and the surface oxyphilicity. Although several studies showed enhanced activity of electrochemical oxidation and oxygen reduction reaction for ternary nanoparticles, i.e., AuPtM (M=Ni, Fe, Cu, Co)[27-32, 33], there have been no studies addressing how the doping of a third metal in PtAu nanoparticles influences the electrocatalytic properties. Earlier examples showed that Au-decorated PtFe nanocatalysts were effective for formic acid oxidation reaction,[28] supporting the feasibility of the hypothesis. Considering that the stability of base metal alloyed catalysts could suffer from base metal leaching in acidic solutions, there have also been studies showing rational selection of base metals could decrease the d-band center, as shown by DFT calculation [34-35]. Indeed, enhanced activity and stability for oxygen reduction reaction have been shown in recent studies Au@PtNi and Ni@Au@PtNi prepared by two-step routes.[29-30, 36]Also, significant suppression of the carbonaceous poisoning for electrocatalytic MOR is reported by depositing Au on PtNi nanoparticles [37]. However, how the nanostructure is controlled in terms of different metal composition, phase structure, surface structure and surface-oxygenated species for enhancing the catalytic activities remains unknown. In one-pot synthesis route, the reduction of Au precursor could proceed PtNi (Scheme S1), favoring Au@PtNi core-shell structure [29-30, 36]. This is undesired if the catalytic synergy of noble metal Au is needed in the catalytic reaction. Based on the calculated surface energy differences, Au (0.0554 eV/Å^2) < fcc Pt (0.1035 eV/Å^2) < fcc Ni (0.1272 eV/Å^2), ((111) plane of fcc structure) [38] we hypothesize that under controlled thermochemical condition for Au-rich core/PtNi-rich shell structure, Au could diffuse from core to shell and Ni from shell to core, leading to the formation of Ni-rich core/PtAu-rich shell structure (Scheme 1). We demonstrate for the first time in this work that the Au-rich core/PtNi-rich shell structure form upon introduction of Ni to AuPt in a controllable ratio can be reconstructed to form Ni-rich core/PtAu-rich shell structure with an enhanced catalytic synergy.

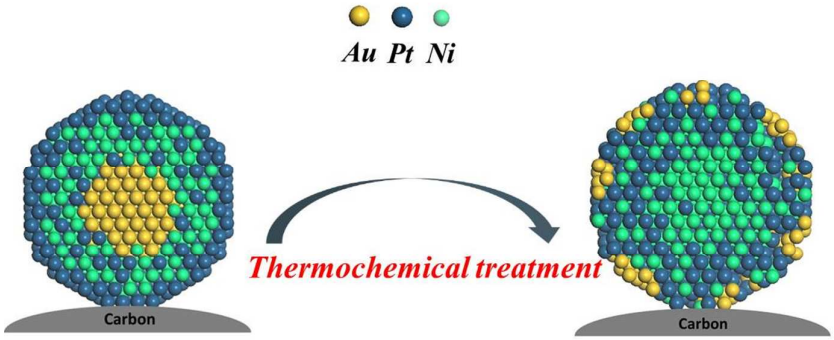

Scheme 1. Reconstruction from Au-rich core/PtNi-rich shell structure to Ni-rich core/PtAu-rich shell structure under controlled thermochemical condition.

2. Experimental Section

Chemicals. Platinum (II) acetylacetonate ($Pt(acac)_2$, 97%) and nickel (II) acetylacetonate ($Ni(acac)_2$, anhydrous, >95%) gold chloride hydrate ($HAuCl_4$) were purchased from Alfa Aesar. 1,2 hexadecanediol (CH_3-$(CH_2)_{13}$-CH(-OH)-CH_2-OH, 90%), octadecene ($CH_3(CH_2)_{15}CH=CH_2$, 99%), oleylamine ($CH_3(CH_2)_7CH=CH(CH_2)_8NH_2$, 70%), oleic acid ($CH_3(CH_2)_7CH=CH(CH_2)_7COOH$, 99%) and Nafion solution (5 wt%) were purchased from Aldrich. Carbon black (Vulcan XC-72) was obtained from Cabot. The Pt/C (from E-tek) catalysts (Pt loading 20%) was obtained from Strem Chemicals. Water was purified with a Millipore Milli-Q water system. Other solvents such as ethanol, hexane and perchloric acid were purchased from Fisher Scientific. All chemicals were used as received.

Catalyst Preparation. Typically, the synthesis of PtAuNi nanoparticles involved mixing three metal precursors, 0.3 mmol $Pt(acac)_2$, 0.4 mmol $Ni(acac)_2$ and 0.14 mmol $HAuCl_4$ with 20 mL octadecene solvent. 1,2-hexadecanediol was added as a reducing agent, and oleic acid and oleylamine as capping agents. Temperature was increased fast (16 ºC/min) to 230 ºC with reflux for 1 h and then cooled to room temperature. NPs were precipitated out by adding ethanol. The PtAuNi NPs were then dispersed in hexane solvent for further use. $Pt_{56}Au_{44}$ nanoparticles were synthesized by the same route using 0.3 mmol $Pt(acac)_2$ and 0.2 mmol $HAuCl_4$. $Pt_{38}Au_{62}$ nanoparticles were synthesized using 0.2 mmol $Pt(acac)_2$ and 0.3 mmol $HAuCl_4$.

The PtAuNi nanoparticles were supported on carbon black and subjected to subsequent thermochemical treatment. The preparation of C-supported nanoparticles followed our earlier

protocols[39] with slight modifications. The thermochemical treatment involved three different conditions, (1) 260 °C in 20 vol% O_2 for 30 min; (2) 177 °C in 20 vol% O_2 for 12 hours; and (3) 400 °C in 15 vol% H_2 for 60 min, to remove the capping agent and anneal the particles.[27, 40]

Transmission electron microscopy (TEM) measurements were carried out on an JEOL JEM 2010F with an acceleration voltage of 200 kV and a routine point-to-point resolution of 0.194 nm. High resolution TEM (HR-TEM) was performed on a TECNAI F-30 transmission electron microscope equipped with a scanning TEM (and STEM) unit and a high-angle annular dark-field (HAADF) detector operated at 300 kV, which has a highest line resolution of 0.100 nm. For TEM measurements, samples were diluted in hexane solution and were drop cast onto a C-coated copper grid followed by solvent evaporation in air.

Ultraviolet−visible spectra were acquired with a HP 8453 spectrophotometer. The spectra were collected in the range of 300−1000 nm.

Inductively Coupled Plasma - Optical Emission Spectroscopy (ICP-OES) were performed on a PerkinElmer 2000 DV ICP-OES instrument utilizing a Mein-hardt nebulizer coupled to a cyclonic spray chamber to increase analytic sensitivity with the following parameters: 18.0 L of Ar(g) min^{-1}; auxiliary 0.3 L of Ar(g) min^{-1}; nebulizer 0.63 L of Ar(g) min^{-1}; power 1500 W; peristaltic pump rate 1.0 mL min^{-1}. Laboratory check standards were analyzed for every 6 or 12 samples and the instrument was recalibrated if the check standards were not within ±5% of the initial concentration.

Thermogravimetric analysis (TGA) was performed on a Perkin-Elmer Pyris 1-TGA.

X-ray powder diffraction (XRD) was used to measure the alloying structures. XRD data was collected from 30 to 90° for 2θ with a step size of 0.5° at room temperature on a Phillips X'pert PW 3040 MPD diffractometer using Cu Kα line (λ= 1.5418 Å), The data was compared to the XRD database of International Centre for Diffraction Data (ICDD) for phase identification.

X-ray photoelectron spectroscopy (XPS) were performed ex situ using a Physical Electronics Quantum 2000 scanning ESCA microprobe. This instrument was equipped with a focused monochromatic Al Kα X-ray (1486.7 eV) source for excitation, a spherical section analyzer and a

16-elementmultichannel detection system. The X-ray beam was approximately 100 μm in diameter. It was rastered over a 1.4 mm by 0.2 mm rectangle spot on the sample. During rastering, the incident X-ray beam was normal to the sample while the X-ray detector tilted at 45° away from the normal. The binding energy (BE) of the chemical species adsorbed at the NP surface was calibrated using the C 1s peak at 284.8 eV as an internal standard. The percentages of the individual elements detected were determined by analyzing the areas of the respective peaks.

Preparation of Working Electrodes. Glassy carbon (GC) disks (geometric area: 0.196 cm^2) were polished with 0.03 μm Al_2O_3 powders, followed by careful rinsing with deionized water. Briefly, the catalysts ink (1 mg/mL) were prepared by ultrasonicating the solution of 5mg catalysts, 4.5 mL distilled water, 0.25 mL isopropanol and 0.25 mL 5 wt% Nafion for 20 min. The as-prepared ink was aging in dark environment for 3 weeks, and then ultrasonicated 20 min. Then, 10 uL of the ink was deposited onto the polished glassy carbon of 5 mm in diameter, followed by drying under ambient condition.

Electrochemical Measurements. Cyclic voltammetry (CV) measurements were performed using a computer-controlled electrochemical analyzer (CHI 600A). The experiments were conducted in three-electrode electrochemical cells at room temperature in 0.1 M $HClO_4$. The reference electrode was silver−silver chloride electrode in saturated KCl (Ag/AgCl (Sat'd KCl)).). The potential can be calibrated to reversible hydrogen electrode (RHE) by the following equation: (E(RHE) = E(Ag/AgCl) + 0.0591pH + E^0(Ag/AgCl)). E^0(Ag/AgCl) is measured to be 0.192 V Cyclic voltammetric sweeps were run at 50 mV/s -0.20-1.25 V or -0.20-1.39 V. MOR was performed in 0.1 M $HClO_4$ containing 0.5 M CH_3OH between -0.20 V and 0.96 V.

Computational modeling. Ab-initio calculations were carried out by DFT as implemented in Dmol3 program coming as a part of Materials Studio software (Accelrys Inc.).[41] Full geometry optimizations were performed for all model atomic configurations tested in this work, in which all atoms were fully relaxed. The configurations included small PtAuNi clusters. The interactions between the model atomic configurations of the clusters and CH_3OH molecule were explored. The energy of adsorption of CH_3OH on the PtAuNi cluster was used as a measure of the strength

of CH_3OH adsorption. It was calculated by $E_{ads} = -(E_{CH_3OH-metal} - E_{metal} - E_{CH_3OH})$, where, $E_{CH_3OH-metal}$, E_{metal} and E_{CH_3OH} are total energy for the CH_3OH-metal complex, the isolated atomic configuration of the cluster, and the isolated CH_3OH molecule, respectively.

3. Results and Discussion

3.1. Compositions and Morphologies

On the basis of our previous work on the MOR activity of Pt_nAu_{100-n} in alkaline electrolyte which showed a gradual increase in activity with decreasing n, reaching a maximum at n ~20,[20] here we focused on Pt_nAu_{100-n} NPs with an intermediate Pt percentage (n ~40) to assess the influence on the activity by replacing a fraction of Au with Ni. A typical example series of such a composition was $Pt_{40}Au_xNi_{60-x}$. The actual trimetallic/bimetallic composition of the NPs were determined by ICP-OES technique, which gave $Pt_{34}Au_2Ni_{64}$ (Sample a), $Pt_{38}Au_8Ni_{55}$ (Sample b), $Pt_{39}Au_{18}Ni_{43}$ (Sample c), $Pt_{40}Au_{30}Ni_{30}$ (Sample d), $Pt_{56}Au_{44}$ (Sample e), and $Pt_{38}Au_{62}$ (Sample f). The mass and atomic percentages of Pt for $Pt_{56}Au_{44}$ and $Pt_{38}Au_{62}$ are similar to those of the other four $Pt_{\sim 40}Au_xNi_{\sim 60-x}$ samples. Figure 1 shows a plot of Au and Ni composition in $Pt_{\sim 40}Au_xNi_{\sim 60-x}$ NPs as a function of nominal feeding in the synthesis. The atomic Au% in the NPs was very close to the Au% in the synthesis feeding. Au and Ni atomic percentages showed a linear relationship with Au feeding percentage. The Ni% decreased and Pt% in the NPs slightly increased with increasing Au feeding percentage.

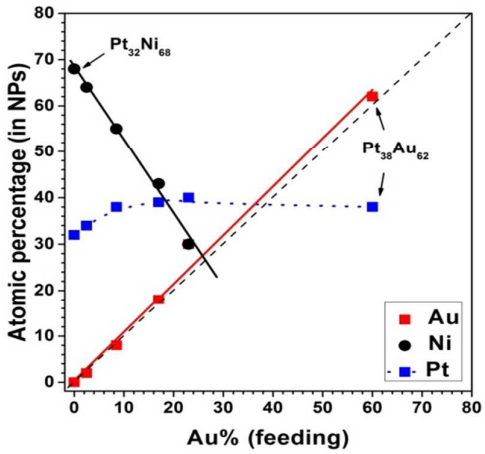

Figure 1. Plots of Au and Ni atomic percentages of $Pt_{\sim 40}Au_xNi_{\sim 60-x}$/C as a function of nominal Au feeding in terms of the atomic percentage.

TEM images of as-synthesized NPs show a spherical morphology with size distribution of 8.7±2.5 nm for Sample e (Figure 2A), 7.0±1.2 nm for Sample d (Figure 2B), and 8.7±2.0 nm for Sample c (Figure 2C, Figure S1). HR-TEM image (Figure 2C inset) reveals distinctive core-shell structure. As shown in Figure 2 D&E for the NPs synthesized by decreasing the Au:Ni ratio, there is a propensity of forming branching structures. In the absence of Au precursor, $Pt_{32}Ni_{68}$ nanoflowers were obtained with a small size feature (Figure S3).

While the lattice fringes from the central part of the particle were complicated by the surface layers of the core, the lattice fringes in the edge of the nanoparticles are not, and thus the difference in lattice fringes measured between the center and edge should reflect the difference of the core and shell. The HR-TEM image (Figure 2F) for as-prepared $Pt_{39}Au_{18}Ni_{43}$ NPs reveals a dark core with lattice fringes of 0.23 nm corresponding to Au (111) plane, and a light shell with lattice fringes of 0.22 nm corresponding to the (111) plane of PtNi-abundant phase. The PtAuNi core-shell structure formation was supported by UV-vis data (see Figure S2) which showed no surface plasmonic band corresponding to Au NPs. This is similar to AuPt core-shell nanoparticles,[24] reflecting the depression of Au SP band by Pt-Ni shells. The standard (111) lattice spacing is 0.235, 0.226 and 0.204 nm for fcc Au, Pt and Ni phases. The interplane distances near the shell is close to Pt's lattice constant, suggestive of Pt surface enrichment. The nanospheres display (111)-dominant facets (interplane distance: 0.21~0.23 nm) and branches with (200) dominant facets (interplane distance: ~0.19 nm) (see Figure S4). Crystalline Au core (interplane distance: 0.23 nm) and PtNi-abundant shell (interplane distance: 0.22 nm and 0.21 nm) are revealed in the initial HR-TEM of a spherical PtAuNi core-shell NP (Figure 2G). The Au core exhibits an increased crystallinity after exposure to high-energy electron beam for 15 min (Figure 2H), at which the difference of interatomic distances between core and shell became smaller. The electron beam induced heating in vacuum, similar to thermal treatment, led to Au surface enrichment.

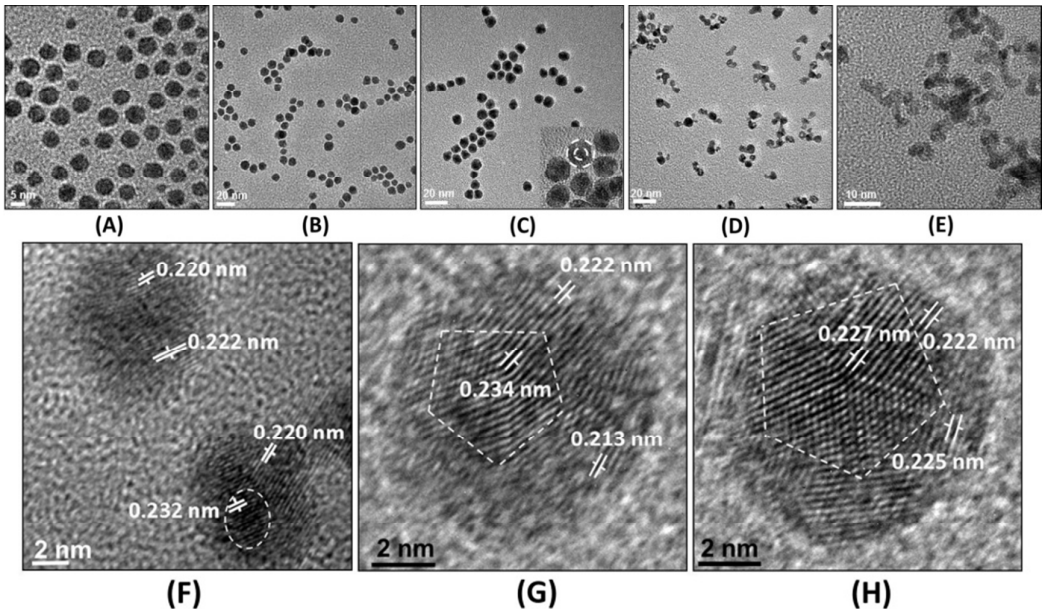

Figure 2. TEM images of as-prepared: (A) $Pt_{56}Au_{44}$, (B) $Pt_{40}Au_{30}Ni_{30}$, (C) $Pt_{39}Au_{18}Ni_{43}$, (inset: High-magnification TEM image showing the contrast of Au core and PtNi shell), (D) $Pt_{37}Au_{8}Ni_{55}$, (E) $Pt_{34}Au_{2}Ni_{64}$ (F) High-resolution TEM image showing the lattice fringes of Au-rich core ((111) lattice space: 0.232 nm) and PtNi-rich shell ((111) lattice space:0.220 nm and 0.222 nm). HR-TEM image of PtAuNi core-shell structure before (G) and after (H) exposure under TEM electron beams for 15 min.

For $Pt_{39}Au_{18}Ni_{43}$/C after thermochemical treatment at 400 ^{o}C under H_2 (400 ^{o}C/H_2), the particles are well dispersed on the carbon (Figure 3A). The corresponding selected area electron diffraction (SAED) pattern (Figure 3A inset) taken from randomly distributed region reveal (111), (200) and (220) diffraction rings of fcc structure. The HR-TEM image (Figure 3B) of a single particle shows the surface Au-rich domains with interatomic distance of 0.23 nm, different from the interplane distance of 0.21 nm in the core regions. Some of the branched NPs were shown to evolve to spherical NPs upon 400 °C/H_2 treatment (Figure S5). Both (200) lattice fringe with interplane distance of 0.19 nm and (111) lattice fringe with interatomic distance of 0.22 nm remain unchanged after in 400^{o}C/H_2 treatment (Figure 3C).

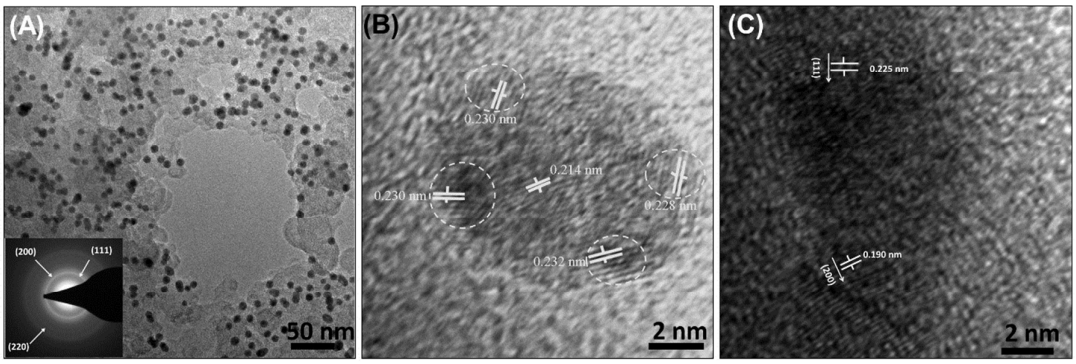

Figure 3. (A) TEM image for 400 °C/H_2 treated $Pt_{39}Au_{18}Ni_{43}$/C (inset: corresponding SAED patterns), (B) HR-TEM image of a single particle with Au-rich surface domain ((111) lattice space: 0.230 nm and 0.232 nm) and PtNi-rich domain (lattice space: 0.214 nm), and (C) HR-TEM image of 400 ºC /H_2 treated $Pt_{37}Au_8Ni_{55}$/C.

The Au-rich core/PtNi-rich shell structure of the as-prepared $Pt_{39}Au_{18}Ni_{43}$/C was also supported by EDS point data that core gave composition of $Pt_{46}Au_{39}Ni_{15}$ and shell gave $Pt_{64}Au_{10}Ni_{25}$ (Figure S6). Figure 4 shows a representative set of HAADF-STEM images and elemental mapping of 400 ^{o}C/H_2 treated $Pt_{39}Au_{18}Ni_{43}$/C. The three elements, Pt, Au and Ni, were all detectable for all individual nanoparticles. Due to the lack of enough resolution of the EDS mapping, the data do not effectively detect the enrichment of a specific element in the NP. However, as shown in Figure 4F, the analysis of the line profile of the 20-nm sized dimeric particles supported the Ni-rich cores. For the smaller ~10 nm particle in the red rectangle region (Figure 4A), EDS data taken from the core site gave a composition of "$Pt_{10}Au_5Ni_{85}$", which is different from the bulk composition of $Pt_{36}Au_{18}Ni_{46}$ (see Figure S8). This result is in consistent with the finding of HR-TEM analysis showing that the 400 ^{o}C/H_2 treated $Pt_{39}Au_{18}Ni_{43}$/C catalyst features Ni-rich core/PtAu-rich shell structure. EDS data of the 260 ºC/O_2 treated $Pt_{39}Au_{18}Ni_{43}$/C catalyst showed a composition of "$Pt_{43}Au_{18}Ni_{28}$" in the core and "$Pt_{37}Au_{14}Ni_{47}$" in the shell (Figure S7), indicative of an enrichment of Ni in the shell. Considering that electron energy loss spectroscopy (EELS) has the ability to detect the composition at 0.5-2 nm of the surface, we plan to use EELS technique to examine the samples in the near future to provide an additional piece of information to further support for the core-shell nanostructure.

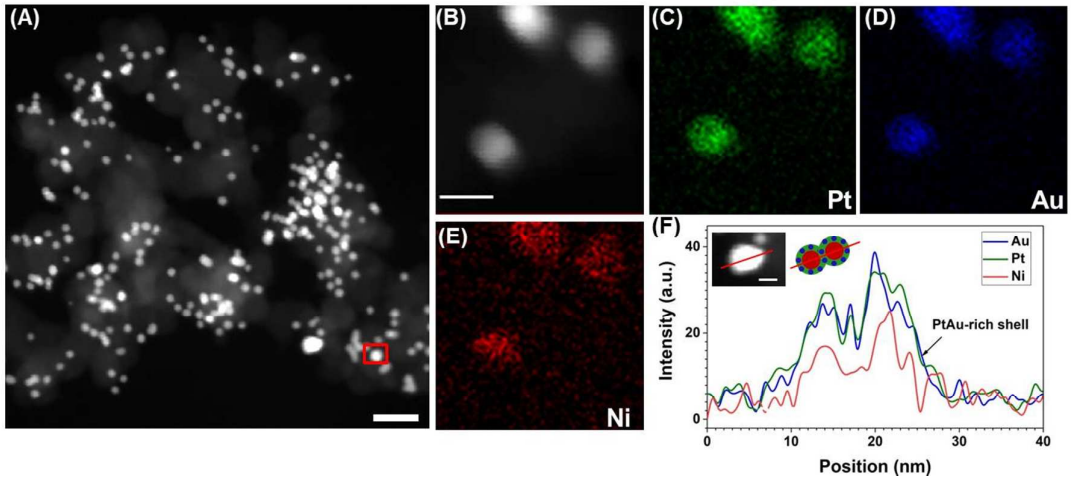

Figure 4. (A) HAADF-STEM image of 400 ºC/H_2 treated $Pt_{39}Au_{18}Ni_{43}$/C. (scale bar: 50 nm): Composition analysis: core composition in the red rectangle region: $Pt_{10}Au_5Ni_{85}$ and bulk composition: $Pt_{36}Au_{18}Ni_{46}$ (see Figure S8 in detail)); (B-F) Elemental mapping showing (C) Pt, (D) Au, (E) Ni. (scale bar: 10 nm). (F) line profile of a larger-sized dimeric particles (inset: HAADF-STEM image and the dimeric model of the particles).

3.2 Phase Properties

XRD pattern of 400 ºC/H_2 treated $Pt_{\sim 40}Au_xNi_{\sim 60-x}$ showed an fcc-type structure (Figure S9A). The structure is influenced by thermochemical treatment (Figure S9B). As shown in Figure 5A, the (111) peak shifts positively with the increase of Ni composition. In comparison with those reported for as-synthesized PtAuFe[42] and PtAu,[6] the characteristic of Au core in our as-synthesized $Pt_{39}Au_{18}Ni_{43}$ NPs was detectable. Catalysts derived from $Pt_{39}Au_{18}Ni_{43}$/C (noted Sample c) treated by three different temperatures, 260 °C/O_2 (noted Sample c-1), 177 °C/O_2 (noted Sample c-2), and 400 °C/H_2 (noted Sample c-3) were examined (Figure 5B). By deconvoluting the XRD peaks for the untreated $Pt_{39}Au_{18}Ni_{43}$ NPs (Sample c), the left shoulder of the main Pt (111) peak can be ascribed to (111) peak of Au core. In terms of Au segregation and Pt-based alloy phase during thermochemical treatment, the XRD spectra between 34° and 50° were deconvoluted into three peaks: Au (111) peak at 38.19° (red curve), Pt alloy (111) peak with a shift (blue curve), and a peak representing the overlap of Au (200) and Pt alloy (200) (green curve). The deconvolution reveals interesting trend: after O_2 treatment at 177 °C, the Au (111) peak was suppressed and the Pt alloy (111) peak shifted negatively from 40.27° to 39.96°. For Sample c-1, the Au (111) peak was weaker while the Pt alloy (111) peak shifted more negatively to 39.75°. The result indicates that PtAu alloying is favored by O_2 treatment, with an expansion

of lattice space. For Sample c-3, Pt alloy (111) peak shifted positively to 40.91°, promoting PtNi alloy with a lattice shrinking. Our previous study showed a relative lattice difference ($\Delta a/a$) of 1.0, 1.4 and 3.0% for Pt, $Pt_{45}Co_{55}$, and $Pt_{50}Co_{25}Ni_{25}$ NPs in O_2 and H_2 treatments.[43] Here, $Pt_{39}Au_{18}Ni_{43}$/C exhibits a significant lattice difference of 2.9 % between the H_2 and O_2 treated sample.

The ratio of Au and Pt alloy (111) peaks represents the ratio of segregated Au vs. Pt alloy phase. For the untreated $Pt_{39}Au_{18}Ni_{43}$/C (noted Sample c), the ratio is 0.195. After 177 °C/O_2 treatment (noted Sample c-2), it decreased to 0.096 so that Au atoms in the core merged into Pt alloy phase. For the 260 °C/O_2 treatment , Au (111) peak is undetectable. The ratio for Sample c-3 is 0.274. Considering the broad Au (111) peak, Au segregation was promoted and converted to very small domains during H_2 treatment.

As demonstrated in Figure 5C, lattice constant for 400 °C/H_2 treated Samples a, b, c, d, e, and f as calculated by Bragg's law, was 0.376, 0.378, 0.381, 0.384, 0.398, and 0.401 nm, respectively. The fcc-type lattice constant for c-1, c-2, c-3, and c ($Pt_{39}Au_{18}Ni_{43}$/C) was 0.392, 0.390, 0.381, 0.387 nm, respectively (Figure 5D). The lattice constants of the four $Pt_{\sim 40}Au_xNi_{\sim 60-x}$/C show linear relationship with Ni% except for $Pt_{38}Au_{62}$/C, demonstrating that Ni doping in PtAu makes significant differences in the crystalline structure. PtNi alloys rather than PtAu alloys are more favored for PtAuNi NPs after 400 °C/H_2 treatment.

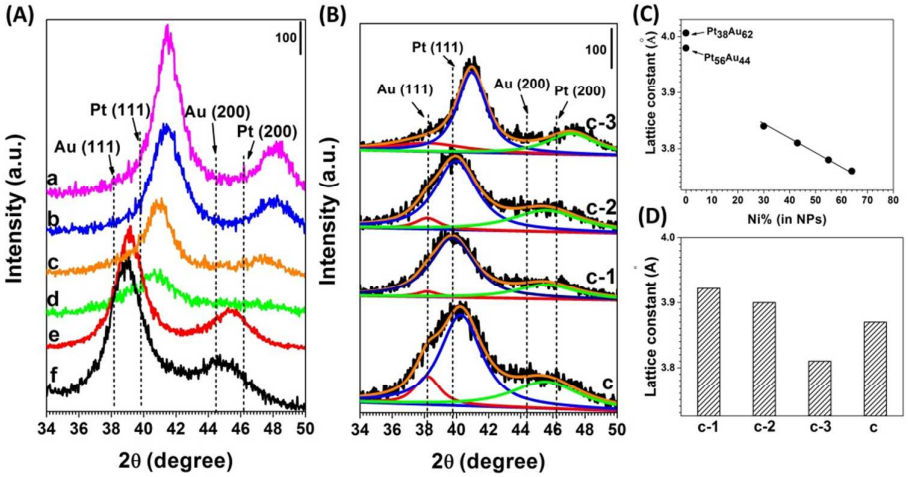

Figure 5. (A) XRD patterns of 400 °C/H_2 treated (a) $Pt_{34}Au_2Ni_{64}$/C, (b) $Pt_{37}Au_8Ni_{55}$/C, (c) $Pt_{39}Au_{18}Ni_{43}$/C, (d) $Pt_{40}Au_{30}Ni_{30}$/C, (e) $Pt_{56}Au_{44}$/C, and (f) $Pt_{38}Au_{62}$/C. (B) Deconvoluted XRD patterns of $Pt_{39}Au_{18}Ni_{43}$/C: (c) as prepared, and treated: (c-1) 260 °C/O_2, (c-2) 177 °C/O_2, and (c-3) 400 °C/H_2. (C) plot of lattice

constant as a function of Ni% for 400 ºC/H_2 treated $Pt_{\sim 40}Au_xNi_{\sim 60-x}$/C. (D) Comparison of lattice constants for c, c-1, c-2, c-3.

The average size of the segregated phase in the NPs can be estimated from the full width at half maximum of Pt (111) peak using Scherer equation:

$$L = \frac{k\lambda}{\beta \cos(\theta)}$$

As shown in Figure S9 C&D, the size for the segregated Pt phase in 400 °C/H_2 treated $Pt_{40}Au_{30}Ni_{30}$/C is 2.2 nm, which is the smallest among the six compositions. For $Pt_{39}Au_{18}Ni_{43}$/C, the size for the segregated Pt phase is shown to decrease from 2.69 nm (as-synthesized) to 2.59 nm after 260 ºC/O_2 treatment, but to increase to 3.95 nm in 400 °C/H_2 treatment.

To further substantiate the structural difference after thermochemical treatments in O_2 and H_2, the in-house XRD data (Figure 6A) were transformed to PDF. As shown in Figure 6B, the lattice constant of 400 ºC/H_2 and 260 ºC/O_2 treated $Pt_{40}Au_{20}Ni_{40}$/C shows 3.853 and 3.954 Å with a difference of 2.6%. In comparison, the 400 °C/H_2 treated $Pt_{56}Au_{44}$/C exhibits a lattice constant of 3.944 Å. The result, consistent with the previous results, has provided clear evidence for the lattice shrinking upon the introduction of Ni atoms into the PtAu NPs.

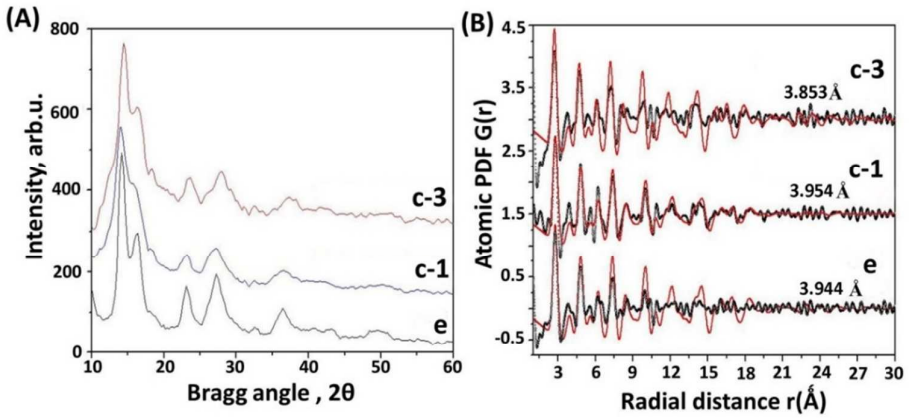

Figure 6. (A) In-house XRD data and (B) corresponding PDF curve for (e) 400 ºC/H_2 treated $Pt_{56}Au_{44}$/C, (c-1) 260 ºC /O_2, and (c-3) 400 ºC /H_2 treated $Pt_{40}Au_{20}Ni_{40}$/C.

The loading of 400 ºC/H_2 treated catalysts (Samples a, b, c, d, e, and f), as determined by TGA, was 23, 25, 23, 16, 27, and 20 wt%, respectively. The actual metal loadings of c-1 and c-2 was 18 and 17 wt%, respectively (Figure S10). Note that Sample c-3 with Au-rich surface

exhibited a higher degree of carbon burning than those of Sample c-1, c-2, reflecting Au being less active than Pt for carbon burning reaction.

3.3 Electrocatalytic Characteristics

CV curves for the 400 ºC/H_2 treated $Pt_{\sim 40}Au_xNi_{\sim 60-x}$/C were performed in N_2 saturated 0.1 M $HClO_4$ (Figure S11A). A typical set of CV curves for the O_2 and H_2 treated $Pt_{39}Au_{18}Ni_{43}$/C is shown in Figure 7A. The waves between -0.19 V and 0.15 V are characteristic of the hydrogen adsorption/desorption,[44] which are broader and weaker compared to those for Pt/C. The peaks observed at 0.25-0.65 V and 0.75-0.95 V correspond to reduction of surface Pt and Au.[6,42] For the samples with high Au content (e.g., $Pt_{39}Au_{18}Ni_{43}$/C c-4, $Pt_{40}Au_{30}Ni_{30}$/C, $Pt_{56}Au_{44}$/C, and $Pt_{38}Au_{62}$/C), the current density showed an increase as the potential is increased above 0.85 V, corresponding to oxidation of Au. For the spherical NPs (e.g., $Pt_{39}Au_{18}Ni_{43}$/C, $Pt_{40}Au_{30}Ni_{30}$/C, and $Pt_{56}Au_{44}$/C), the reduction peak appears at 0.40 V, which showed a downshift to 0.35 V for $Pt_{38}Au_{62}$/C. For the branched NPs ($Pt_{34}Au_2Ni_{64}$/C, $Pt_{38}Au_8Ni_{55}$/C), it appears at about 0.47 V. The peak positions depend on the thermal treatment. For Sample c-1 and c-2, the reduction peak appeared at 0.43 and 0.45 V, respectively, which is higher than that of Sample c-3. The suppression of Au reduction peak for O_2 treated $Pt_{39}Au_{18}Ni_{43}$/C was due to the absence of surface Au atoms. As a comparison, the 400 ºC/H_2 and 260 ºC/O_2 treated $Pt_{56}Au_{44}$/C catalysts were subjected to the identical electrochemical measurement (Figure S12 A&B).

The measurements of MOR were carried out in N_2-saturated 0.1 M $HClO_4$ solution with 0.5 M MeOH (Figure 7B-C, Figures S11B & S13). The well-defined peaks in the forward sweep correspond to the electrochemical oxidation of methanol with the formation of carbonaceous species adsorbed on the surface of catalyst. The backward peaks reflect the oxidation of the carbonaceous species.[45] The MOR activity clearly depends on the composition, thermochemical and electrochemical treatments. MOR properties of $Pt_{39}Au_{18}Ni_{43}$/C also vary significantly with treatment. Sample c-4 was 400 ºC/H_2 treated $Pt_{39}Au_{18}Ni_{43}$/C subjected to potential cycling to a higher potential, and exhibited the strongest forward wave based on Pt mass (Figure 7B), whereas Sample c-3 showed the strongest MOR feature based on surface active area (Figure 7C). Both the

O_2 and H_2 treated $Pt_{39}Au_{18}Ni_{43}$/C showed much higher activities than that of Pt/C.

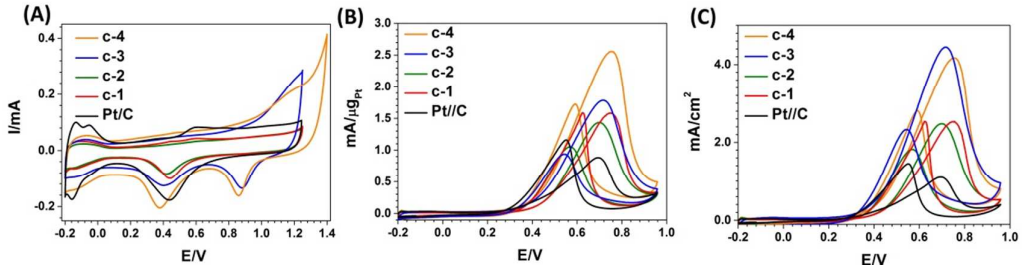

Figure 7. CV curves for (c-1) 260 ºC/O_2, (c-2) 177 ºC/O_2, (c-3) 400 ºC/H_2 treated $Pt_{39}Au_{18}Ni_{43}$/C in comparison with Pt/C in (A) 0.1 M $HClO_4$, and (B, C) 0.1 M $HClO_4$ + 0.5 M MeOH in terms of mA/μg (Pt) and mA/cm^2 (Pt). Sample c-4 (i.e., 400 ºC/H_2 treated $Pt_{39}Au_{18}Ni_{43}$/C) was subjected to potential cycling to a higher potential (1.39 V).

Electrochemical active area (ECA) was measured by integration of the charges under the hydrogen adsorption waves between -0.20 V and 0.10 V. Figure 8A shows ECA values of 400 °C/H_2 treated Sample a, b, c, d, e, f ($Pt_{\sim 40}Au_xNi_{\sim 60-x}$/C, $Pt_{56}Au_{44}$/C, $Pt_{38}Au_{62}$/C), which are lower than that of Pt/C (80 m^2/g_{Pt}). ECA values for c-1, c-2, c-3 ($Pt_{39}Au_{18}Ni_{43}$/C) are 63, 58 and 40 m^2/g_{Pt}. Sample c-4 exhibits a higher ECA (65 m^2/g_{Pt}) compared to Sample c-3 (Figure S14), reflecting an increased level of Ni leaching due to the potential cycling. The ECA values of 260 ºC/O_2, 400 ºC/H_2 treated $Pt_{56}Au_{44}$/C are 47 and 30 m^2/g_{Pt}, respectively, which increase to 48 and 60 m^2/g_{Pt} after experiencing a higher potential of 1.39 V.

The ECA can also be evaluated based on surfaced Au, ECA_{Au}, by the following equation:

$$ECA_{Au} = \frac{Q}{340\ \mu C/cm^2\ m_{Au}}$$

where m_{Au} is the total mass of Au, and Q is the total charge which can be evaluated by the area of Au reduction peak. ECA_{Au} exhibit a maximum value of 65 m^2/g_{Au} for 400 ºC/H_2 treated $Pt_{39}Au_{18}Ni_{43}$/C (Figure 8A). Due to uniform distribution of Au atoms on the surface, $Pt_{39}Au_{18}Ni_{43}$/C showed the highest values of ECA_{Pt} and ECA_{Au}.

Considering the leaching of surface Ni in the process of potential cycling, the surface Pt:Au ratio is a critical parameter influencing the electrocatalytic properties. The surface Pt percentage of (Pt/(Pt+Au)) can be calculated using the area of hydrogen adsorption waves and Au reduction peak[6] (Figure S15), which showed a linear relationship with atomic Ni% (Figure 8B), except for $Pt_{56}Au_{44}$/C and $Pt_{38}Au_{62}$/C. In addition, as reflected by the values for the 400 ºC/H_2 treated

$Pt_{39}Au_{18}Ni_{43}$/C and $Pt_{56}Au_{44}$/C after potential cycling to 1.39 V (60% and 57%) being lower than that of 260 °C/O_2 treated $Pt_{56}Au_{44}$/C (81.25% and 82.9%) after potential cycling to 1.25 and 1.39 V, the O_2 treatment appeared to favor surface Pt enrichment than that of H_2 treatment.

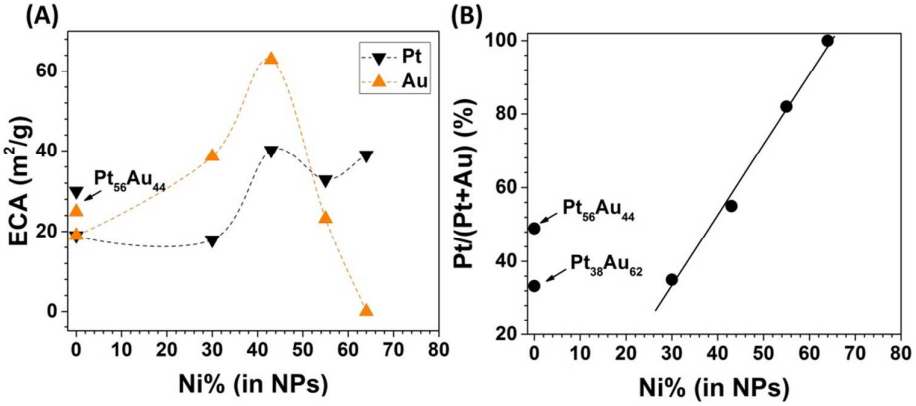

Figure 8. Plots of ECA_{Pt} and ECA_{Au} values) vs. Ni% for 400 ºC/H_2 treated $Pt_{\sim 40}Au_xNi_{\sim 60-x}$/C and $Pt_{56}Au_{44}$/C per Pt or Au mass based on hydrogen adsorption wave or Au reduction peak (A), and surface Pt/(Pt+Au) measured from CV curve based on Au reduction peak) vs. Ni%(B).

As shown in Figure 9A, the mass activities (MA) at 0.6 V for the 400 °C/H_2 treated catalysts are compared with that of Pt/C, showing increases by a factor as high as 2.4 for Sample c-4. The specific activities (SA) at 0.6 V are also compared with Pt/C, showing increases by a factor as high as 4.0. For 400 ºC/H_2 treated $Pt_{\sim 40}Au_xNi_{\sim 60-x}$/C, a higher Ni content tends to exhibit a higher activity. The 400 °C/H_2 treated catalysts with an intermediate atomic Ni% ($Pt_{39}Au_{18}Ni_{43}$) showed an enhanced activity, as evidenced by the maximum MA and SA at practically the same atomic Pt% in the NPs (Figures 9B). Considering the activities of Au NPs[46] and AuPt[6, 7] for MOR, the high activity of the 400 ºC/H_2 treated $Pt_{39}Au_{18}Ni_{43}$/C is believed to be linked to the high values of ECA_{Pt} and ECA_{Au}. The forward peak potential shows a similar trend in terms of MA and SA showing a maximum value at the intermediate Ni% (Figure S16).

The ratio of forward vs. backward maximum current (J_f/J_b) represents the tolerance of catalyst to the carbonaceous species. As shown in Figure 9C, J_f/J_b values of 400 ºC/H_2 treated catalysts, in comparison with Pt/C, are shown to decrease with Ni atomic percentage. Note that J_f/J_b for $Pt_{56}Au_{44}$/C shows a low value. The presence of Ni in PtAu clearly increased the tolerance to the carbonaceous species, in addition to the ability of surface Au atoms to suppress carbonaceous species (Figure S17).

As shown in Figure 9D for $Pt_{39}Au_{18}Ni_{43}/C$, the MA shows a clear increase in comparison with Pt/C. Sample c-4 exhibited larger ECA and MA but smaller SA than c-3, reflecting surface Pt enrichment for c-4 and a stronger negative charge sink effect.[47] Ni leaching leads to a smaller SA. For $Pt_{56}Au_{44}/C$. 400 ºC/H_2 treated $Pt_{56}Au_{44}/C$ (Figure S18), the MA is lower than that for the 260 ºC/O_2 treated $Pt_{56}Au_{44}/C$. Potential cycling to a higher potential increases both SA and MA for the 400 ºC/H_2 treated sample. The fact that the activities of $Pt_{56}Au_{44}/C$ and $Pt_{38}Au_{62}/C$ are much lower than $Pt_{39}Au_{18}Ni_{43}/C$ reflect the important role of Ni in the PtAu NPs in terms of catalytic synergy.

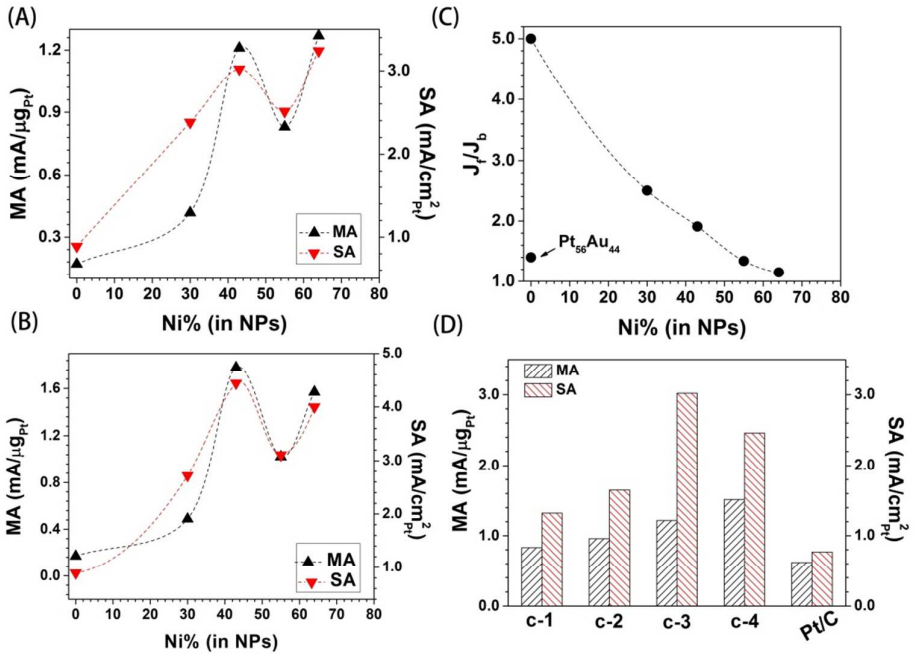

Figure 9. Plots of MA and SA at peak potential at 0.6 V (A) and at peak potential forward sweep (B), as well as J_f/J_b (C) as a function of Ni% for 400 ºC/H_2 treated $Pt_{\sim 40}Au_xNi_{\sim 60-x}/C$; (D) Comparison of MA and SA (at 0.6 V) for $Pt_{39}Au_{18}Ni_{43}/C$ after different treatments: (c-1) 260 ºC/O_2, (c-2) 177 ºC/O_2, (c-3) 400 ºC/H_2, and (c-4) 400 ºC/H_2 treatment and potential cycling to 1.39 V.

In comparison with most binary catalysts reported in the literature (see Table S1), the data for our catalysts showed much enhanced performances. For example, the SA ratio for our $Pt_{39}Au_{18}Ni_{43}/C$ vs. Pt/C is 3.92 with J_f/J_b of 1.91, which is much larger than that of $Pt_{50}Au_{50}$ (SA ratio 2.2 with J_f/J_b of 1.1).[6] For PtNi ribbons, the MA vs. Pt/C and J_f/J_b value are much lower than $Pt_{39}Au_{18}Ni_{43}/C$.[17] The MA and SA for hollow PtCu NPs are 3.73 and 4.46 times higher than those for Pt/C, whereas its J_f/J_b value is 1.0, which is much lower than that of $Pt_{39}Au_{18}Ni_{43}/C$.

The stability of the $Pt_{39}Au_{18}Ni_{43}$/C catalysts was also investigated (Figure S19 A-B). For Samples c-4 and c-3 after a decrease in the first 30 potential cycles, MA was found to remain unchanged at above 1.8 and 1.4 $mA/\mu g_{Pt}$. For Samples c-1 and c-2, MA showed a decrease in the first 15 cycles and remained unchanged at about 1.1 and 1.2 $mA/\mu g_{Pt}$. The J_f/J_b remained largely unchanged in comparison with Pt/C. These results demonstrate that the high stability could be maintained with an optimal level of Ni in the AuPt nanoparticles, a detailed investigation of the stability evolution process is beyond the scope of this report, which will be reported in the near future.

3.4 Changes in Surface Composition

It is evident that the MOR activities of $Pt_{39}Au_{18}Ni_{43}$/C catalysts depend strongly on the electrochemical and thermochemical treatment, which were examined by XPS to assess the surface valent state and composition. Figure 10 A-B shows a set of XPS spectra in the Ni $2p_{3/2}$ region. By spectral deconvolution, there are three peak components of Ni 2p: peak (I) (light blue curves) can be ascribed to Ni^0 alloyed with Pt; peak (II) (pink curves) as well as the satellite peaks (III) (dark yellow curves) correspond to Ni-O species.[48-50] Sample c-1 shows a strong Ni-O peak, and Sample c-2 shows a weaker Ni-O peak. Ni-O is favored by O_2 treatment. Peaks (II) and (III) of the O_2 treated Sample c-1, c-2 were greatly suppressed after potential cycling (Figure 10 B), indicating the removal of Ni-O species.

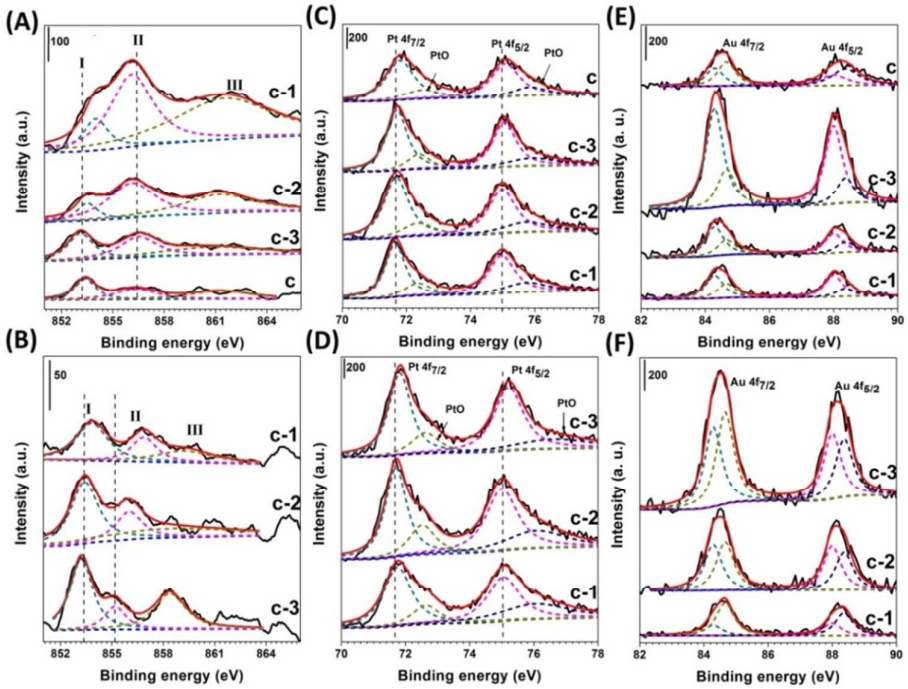

Figure 10. XPS spectra (and deconvoluted peaks) for (c) as-synthesized, and (c-1) 260 ºC/O_2, (c-2) 177 ºC/O_2, and (c-3) 400 ºC/H_2 treated $Pt_{39}Au_{18}Ni_{43}$/C, in regions of Ni 2p (A, B), Pt 4f (C, D), and Au 4f (E, F), before (A, C, E) and after (B, D, F) cycling at 50 mV/s between -0.20 and 1.25 V in 0.1 M $HClO_4$ for 10 cycles.

The deconvolution of Pt 4f spectra yields two set of peaks (Figure 10 C and D): the first set corresponds to Pt^0 $4f_{7/2}$ and Pt^0 $4f_{5/2}$ and the second, with a shift on the right shoulder, can be ascribed to PtO $4f_{7/2}$ and PtO $4f_{5/2}$.[50-51] As shown in Figure 10 E and F, the deconvolution of the Au $4f_{7/2}$ and Au $4f_{5/2}$ spectra also yields two sets of peaks (84.29, 84.66 eV and 88.0, 88.37 eV with the same FWHM of 0.65 eV, except for the untreated $Pt_{39}Au_{18}Ni_{43}$/C, its FWHM is 1.0 eV). In the region of Au $4f_{7/2}$,[52] the ratio of peak areas at 84.66 and 84.29 eV is 0.52, 0.62, 0.38, and 1.34 for Samples c-1, c-2, c-3, and c, respectively. Due to under coordination of the surface atoms, surface Au atoms exhibit a lower BE band than those underneath them.[53] After potential cycling, the ratios were shown to increase significantly to 3.16, 1.06, and 1.15 for Sample c-1, c-2, and c-3, reflecting the oxidation of considerable Au atoms, which promotes MOR effectively.

Based on the XPS analysis of the peak areas of Pt 4f, Au 4f, and Ni 2p (Table S2), the relative surface compositions were found to be $Pt_{57}Au_{14}Ni_{28}$, $Pt_{35}Au_{14}Ni_{50}$, $Pt_{50}Au_{20}Ni_{30}$, and $Pt_{42}Au_{42}Ni_{16}$ for Samples c, c-1, c-2, and c-3, respectively. The untreated sample showed less surface Ni and Au content compared to the bulk composition. This observation is consistent with

a core-shell structure with Ni interior and Pt surface enrichments. Sample c-3 shows significantly higher Au content than the bulk composition and equal surface composition of Pt and Au, which is consistent with the HAADF-STEM mapping result. Because of the surface energy difference (fcc Au < fcc Pt < fcc Ni), the diffusions of Au atoms from core to shell and Ni atoms from shell to core were favored during thermal treatment under H_2, leading to the transformation of the Au-rich core/PtNi-rich shell structure to the Ni-rich core/PtAu-rich shell structure. After potential cycling, the relative surface compositions of Samples c-1, c-2, and c-3 were found to $Pt_{57}Au_{28}Ni_{14}$, $Pt_{66}Au_{22}Ni_{11}$, $Pt_{50}Au_{40}Ni_{10}$, showing 72%, 63%, and 37% loss of surface Ni compared to those before the cycling. It appeared that PtAu-rich surface inhibits Ni leaching during potential cycling.

The Ni $2p_{3/2}$ peak (I) for sample c-1 appears at 854.00 eV, higher than 853.50 eV and 853.10 eV for Samples c-2 and c-3. The peak (II) position for Sample c-3 is higher than that of O_2 treated c-1 and c-2. After potential cycling, Ni $2p_{3/2}$ peak (I) for all samples shifted negatively corresponding to the removal of surface Ni-O. Different from Ni^0 2p, the peak position for Pt^0 $4f_{7/2}$ and $4f_{5/2}$, and Au $4f_{7/2}$ and $4f_{5/2}$ are shown to be shifted positively after potential cycling, indicative of the positively charged surface PtAu species. The Pt^0 $4f_{7/2}$ and $4f_{5/2}$ peak positions display the order of c-3 > c-2 > c-1, whereas the Au $4f_{7/2}$ and $4f_{5/2}$ peak positions of Sample c-3 are lower than those of Samples c-1 and c-2. The surface Pt in Sample c-3 appears to undergo the most electron charge transfer to the neighboring Au atoms, leading to d-charge depletion and thus increasing d-holes of Pt. The Pt with a higher d-charge depletion tends to show higher activity in catalyzing MOR. In our previous study, the Pt $4f_{7/2}$ and Pt $4f_{5/2}$, and Au $4f_{7/2}$ and Au $4f_{5/2}$ for 400 ºC/H_2 treated $Pt_{78}Au_{22}$/C were found at 71.9 and 75.25, and 84.45 and 88.10 eV, respectively,[54] which were more positive than those of Samples c-1, c-2 and c-3.

3.5 Mechanistic Consideration

Taken together, the trimetallic PtAuNi NPs have been shown to undergo surface reconstruction by thermochemical and electrochemical treatments in terms of relative surface enrichment and alloying, which have played an important role in enhancing the electrocatalytic

performance for MOR. Scheme 1 depicts the structural evolution of $Pt_{39}Au_{18}Ni_{43}$ NPs, which occurs during the thermochemical treatment and potential cycling. For the 400 ºC/H_2 treatment, Au atoms move towards the surface, promoting the formation of PtNi alloy. Note that PtNi NPs with ~1:1 Pt:Ni ratio is the most active for PtNi alloy in acidic solution.[55] Under the O_2 treatment (Scheme S2), the formation of surface Ni-O species induces the diffusion of Ni atoms toward the surface. The partially oxidized Ni species would suppress the formation of PtNi alloy. In the potential cycling, a great part of surface Ni atoms on the O_2-treated $Pt_{39}Au_{18}Ni_{43}$ NPs dissolves, whereas for the 400 ºC/H_2 treated $Pt_{39}Au_{18}Ni_{43}$ NPs the Ni dissociation was suppressed by the surface Au and PtAu components with positive partial charges.

To understand the composition-driven optimization of activity for $Pt_{\sim 40}Au_{60-n}Ni_{\sim n}$, DFT calculations were performed based on small PtAuNi cluster models of different compositions ($Pt_4Au_{6-n}Ni_n$ clusters (n=1~ 6)) after optimization. Molecular adsorption of CH_3OH on the model clusters were evaluated on the basis of the optimal bridge or atop adsorption model (Figure 11). The results from geometry optimization of the clusters revealed that Au atom tends to occupy on vertex site and Ni atom on bridge site. The computation results showed that CH_3OH molecule prefers to adsorb on Pt atop site of the model clusters via O atom. The variation of the adsorption energy of CH_3OH on the clusters vs. the cluster composition is shown in Figure 11, revealing two lowest adsorption energies corresponding to the clusters of $Pt_{40}Au_{20}Ni_{40}$ and $Pt_{40}Ni_{60}$. It is evident that the trend in this plot coincides with the trend observed for the MOR activity. Generally speaking, if two reactants share the same transition state, the reactant with a higher adsorption energy would have a higher reaction barrier. Therefore, the adsorption of CH_3OH on $Pt_4Au_{6-n}Ni_n$ clusters with a higher adsorption energy could have a lower activity. Apparently, for $CH_3OH/Pt_{40}Au_{20}Ni_{40}$ and $CH_3OH/Pt_{40}Ni_{60}$, the lower adsorption energy means a higher activity. As shown in Figure 11, this theoretical finding is clearly in agreement with the experimental data.

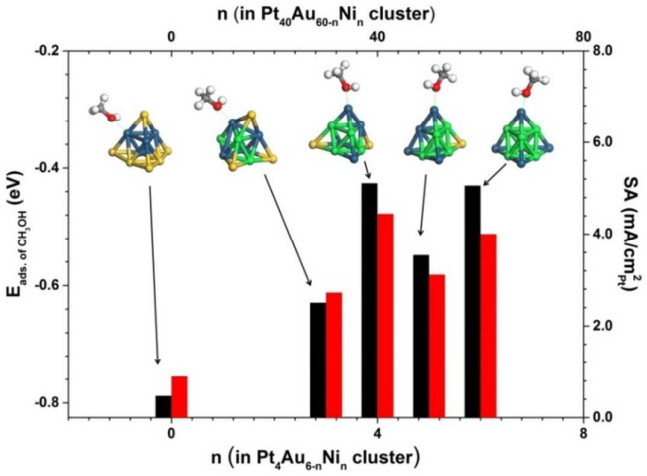

Figure 11. Plot of the DFT-calculated adsorption energy for CH_3OH adsorbed on $Pt_4Au_{6-n}Ni_n$ clusters (n=1~ 6) (black bar) and SA of forward peak (red bar) vs. the normalized composition, with the corresponding CH_3OH / $Pt_4Au_{6-n}Ni_n$ structures shown in the top panel.

Considering the surface evolution and catalytic activity for the 400 ºC/H_2 treated $Pt_{39}Au_{18}Ni_{43}$ NPs and the lowest reaction energy determined by the DFT calculation for MOR in terms of the predominant indirect pathway.[56-57] Scheme 2 depicts a possible sequence of the formation surface species that could be linked to the surface catalytic sites and synergy, including CH_3OH_{ad}, CH_2OH_{ad}, $CHOH_{ad}$, CHO_{ad}, and CO_{ad}. In terms of cleavage of C-H and O-H bonds of methanol, the activation could be favored by the shrinking of Pt-Pt interatomic distance as a result of the PtNi alloying. The electrons generated in each of the dehydrogenation stages could be extracted by the neighboring surface Au atoms with partial positive charges. In contrast to a strong triple bond between CO and Pt[57] which poisons the catalytic sites, the CO species on Pt sites could be removed to the Au sites forming a weaker atop adsorption bond, which is reminiscent of the role of Au in AuPt nanoparticles for MOR.[20] For the NPs with a surface atomic ratio of Pt:Au ~ 1:1 obtained after electrochemical activation, there is an optimal activity for MOR. The transfer of CO species to Au site is followed by reaction with OH_{ad} species toward CO_2 product. In these processes, the partially-positive charged Au sites serve enables maneuvering of the electrons involved in the oxidation reactions. Moreover, the transfer of electrons from Ni with a lower electronegativity (1.91) to Pt with a higher electronegativity (2.28) in PtNi alloy would lower the d-band center of Pt, [17, 58-59] which suppress the strong adsorption of carbonaceous in each step. It is the introduction of Ni into the bimetallic NPs that has produced

the above multifunctional synergy involving shrinking of Pt-Pt distances for enhancing the dehydrogenation and surface enrichments of Au and PtNi alloy phases for effective removal surface carbonaceous species and maneuvering of the electrons. We note that a detailed study of the CO oxidation on PtAuNi is part of our on-going investigation, which will be reported in the near future.

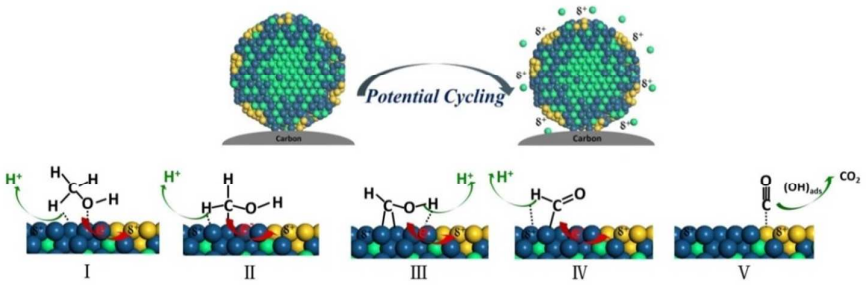

Scheme 2. Top panel: an illustration of the surface reconstruction of 400 ºC/H_2 treated $Pt_{39}Au_{18}Ni_{43}$ NPs upon electrochemical potential cycling. Bottom panel: a possible sequence of the formation of surface species that could be linked to the surface catalytic sites and synergy (CH_3OH_{ad} (I), CH_2OH_{ad} (II), $CHOH_{ad}$ (III), CHO_{ad} (IV), and CO_{ad} (V)) in an indirect pathway for the electrocatalytic MOR over the catalyst.

4. Conclusion

In conclusion, we have demonstrated that the introduction of a third low-cost nickel into AuPt nanoparticles followed by thermochemical and electrochemical tuning leads to a significant enhancement for the catalytic activity for methanol oxidation reaction. The unique combination of composition-controlled synthesis and thermochemical/electrochemical reconstruction of metal components on the surface and in the interior of the nanoparticles has enabled the tuning of electrocatalytic properties. In comparison with the general approach to design catalysts based on the bimetallic PtAu NPs, the introduction of Ni into the bimetallic NPs is shown to produce a significant multifunctional synergy. This synergy involves alloying of Ni with Pt to shrink the Pt-Pt distances which enhances the catalytic dehydrogenation, and to induce surface enrichments of Au which promotes effective removal of surface carbonaceous species and enables the Au atoms function as an electron sink for maneuvering of the electrons involved in the oxidation reaction. To achieve the multifunctionality, the thermochemical and electrochemical treatments of the core-shell PtAuNi NPs are shown to contribute to the controllability of the surface enrichment that

plays a critical role in the electrocatalytic enhancement. The thermochemical treatment under hydrogen favors surface enrichment of Au and core enrichment of Ni, which increase the efficiency of noble metal in the alloy, optimize the d-band electronic properties of Pt, and promote the multifunctional synergy. The experimentally-observed electrocatalytic activity of the nanocatalysts in terms of Ni doping in PtAu nanoparticles is further supported by the results of theoretical analysis of the adsorption energy of methanol on the nanoclusters, revealing that the higher activity correlates well with the lower adsorption energy. These findings have provided new insights into the design and preparation of highly active electrocatalysts. We also note that an expansion of work to the study of the structural modifications of the catalysts for other electrocatalytic reactions, e.g., oxygen reduction reaction,[60-63] is also an important direction of future studies.

Supporting Information

The Supporting Information is available, which includes additional TEM images, Size distribution analysis; EDS data; UV−vis spectra; TGA data; XRD data; CV data; Plots in terms of size, ECA, MA, SA, and J_f/J_b; and Comparisons with literature data.

Acknowledgements

This work was supported by DOE-BES Grant (DE-SC0006877) and NSF Grant (CHE 1566283). The authors thank Professor David Jenkins of Binghamton University for his great help in the XRD measurements.

References

1. Ren, X. M.; Zelenay, P.; Thomas, S.; Davey, J.; Gottesfeld, S. *J. Power Sources* **2000**, *86*, 111-116.
2. Chu, D.; Jiang, R. *Solid State Ionics* **2002**, *148*, 591-599.
3. Paulus, U. A.; Endruschat, U.; Feldmeyer, G. J.; Schmidt, T. J.; Bonnemann, H.; Behm, R. J. *J. Catal.* **2000**, *195*, 383-393.
4. Antolini, E. *Mater. Chem. Phys.* **2003**, *78*, 563-573.
5. Lu, G. Q.; Wieckowski, A. *Curr. Opin. Colloid Interface Sci.* **2000**, *5*, 95-100.
6. Suntivich, J.; Xu, Z.; Carlton, C. E.; Kim, J.; Han, B.; Lee, S. W.; Bonnet, N.; Marzari, N.; Allard, L. F.; Gasteiger, H. A.; Hamad-Schifferli, K.; Yang, S. -H. *J. Am. Chem. Soc.* **2013**, *135*, 7985−7991.
7. Luo, J.; Njoki, P. N.; Lin, Y.; Mott, D.; Wang, L.; Zhong C. J. *Langmuir*, **2006**, *22*, 2892–2898.
8. Lu, C.; Kong, W.; Zhang, H.; Song, B.; Wang Z. *J. Power Sources* **2015**, *296*, 102−108.
9. Meyer, R.; Lemire, C.; Shaikhutdinov, S. K.; Freund, H.-J. *Gold Bull.* **2004**, *37*, 72–124.
10. Luo, J.; Maye, M. M.; Lou, Y.; Han, L.; Hepel, M.; Zhong, C. J. *Catal. Today* **2002**, *77*, 127−138.
11. Maye, M. M.; Lou, Y.; Zhong, C. J. *Langmuir* **2000**, *16*, 7520–7523.
12. Petkov, V.; Wanjala, B. N.; Loukrakpam, R.; Luo, J.; Yang, L.; Zhong, C. J.; Shastri, S. *Nano lett.* **2012**, *12*, 4289−4299.
13. Borkowska, Z.; Tymosiak-Zielinska, A.; Nowakowski, R. *Electrochim. Acta* **2004**, *49*, 2613−2621.
14. Tang, H.; Chen, J. H.; Wang, M. Y.; Nie, L. H.; Kuang, Y. F.; Yao, S. Z. *Appl. Catal., A* **2004**, *275*, 43−48.
15. Umeda, M.; Ojima, H.; Mohamedi, M.; Uchida, I. J. *J. Power Sources* **2004**, *136*, 10−15.
16. Kitchin, J. R.; Nørskov, J. K.; Barteau, M. A.; Chen J. G. *J. Chem. Phys.* **2004**, *120*, 16613–16617.
17. Xu, C.; Hou, J.; Pang, X.; Li, X.; Zhu, M.; Tang B. *Int. J hydrogen energy* **2012**, *37* 10489−10498.
18. Nassr, A. B. A. A.; Sinev, I.; Pohl, M.-M.; Grünert, W.; Bron, M. *ACS Catal.* **2014**, *4*, 2449−2462.
19. Papadimitriou, S.; Armyanov, S.; Valova, E.; Hubin, A.; Steenhaut, O.; Pavlidou, E.; Kokkinidis, G.; Sotiropoulos, S. *J. Phys. Chem. C* **2010**, 114, 5217–5223
20. Mott, D.; Luo, J.; Njoki, P. N.; Lin, Y.; Wang, L.; Zhong C. J. *Catal. Today* **2007**, *122*, 378−385.
21. Luo, J.; Maye, M. M.; Kariuki, N. N.; Wang, L.; Njoki, P.; Lin, Y.; Schadt, M.; Naslund, H.

R.; Zhong, C. J. *Catal. Today* **2005**, *99*, 291−297.

22. Yang, L.; Yang, W.; Cai Q. *J. Phys. Chem. C* **2007**, *111*, 16613-16617.
23. Yan, J.-M.; Zhang, X.-B.; Akita, T.; Haruta, M.; Xu Q. *J. Am. Chem. Soc.* **2010**, *132*, 5326–5327.
24. Luo, J.; Wang, L.; Mott, D.; Njoki, P. N.; Lin, Y.; He, T.; Xu, Z.; Wanjana, B. N.; Lim, I.-I. S.; Zhong, C. J. *Adv. Mater.* **2008**, *20*, 4342–4347.
25. Zhang, J.; Sasaki, K.; Sutter, E.; Adzic R. R. *Science* **2007**, *315*, 220–222.
26. Wanjala, B. N.; Luo, J.; Loukrakpam, R.; Fang, B.; Mott, D.; Njoki, P. N.; Engelhard, M.; Naslund, H. R.; Wu, J. K.; Wang, L.; Malis, O.; Zhong, C. J. *Chem. Mater.* **2010**, *22*, 4282–4294.
27. Wang, C.; Vliet, D.; More, K. L.; Zaluzec, N. J.; Peng, S.; Sun, S.; Daimon, H.; Wang, G.; Greeley, J.; Pearson, J.; Paulikas, A. P.; Karapetrov, G.; Strmcnik, D.; Markovic, N. M.; Stamenkovic, V. R. *Nano Lett.* **2011**, *11*, 919–926.
28. Cai, Z.; Lu, Z.; Bi, Y.; Li, Y.; Kuang, Y.; Sun X. *Chem. Commun.*, **2016**, *52*, 3903−3906.
29. Kang, Y.; Snyder, J.; Chi, M.; Li, D.; More, K. L.; Markovic, N. M.; Stamenkovic, V. R. *Nano Lett*. **2014**, *14*, 6361−6367.
30. Shi, Q.; Zhu, C.; Fu, S.; Du, D.; Lin Y. *ACS Appl. Mater. Interfaces*. **2016**, *8*, 4739−4744.
31. Sun, X., Li D.; Ding Y.; Zhu W.; Guo S., Wang Z. L.; Sun S. *J. Am. Chem. Soc.* **2014**, 136(15), 5745–5749.
32. Tan, X.; Prabhudev, S.; Kohandehghan, A.; Karpuzov, D.; Botton, G. A.; Mitlin D. *ACS Catal*. **2015**, 5, 1513−1524
33. Dutta, A.; Ouyang J.; *ACS Catal.* **2015**, *5*, 1371−1380.
34. Xu, C.; Hou, J.; Pang, X.; Li, X.; Zhu, M.; Tang B. *Int. J. Hydrogen Energy* **2012**, *37*, 10489−10498.
35. Zhu, E.; Li, Y.; Chiu, C.-Y.; Huang, X.; Li, M.; Zhao, Z.; Liu, Y.; Duan, X.; Huang, Y. *Nano Res*. **2016**, *9*: 149–157.
36. Shen, L.-L.; Zhang, G.-R.; Miao, S.; Liu, J.; Xu B.-Q. *ACS Catal*. **2016**, *6*, 1680−1690.
37. Wu, Y.; Wang, D.; Zhou, G.; Yu, R.; Chen, C., Li Y. *J. Am. Chem. Soc.* **2014**, 136, 11594−11597
38. Wan, J.; Fan, Y. L.; Gong, D. W.; Shen, S. G.; Fan X. Q. *Model. Simul. Mater. Sci. Eng.* **1999**, *7*, 189–206.
39. Yang, L.; Shan, S.; Loukrakpam, R.; Petkov, V.; Ren, Y.; Wanjala, B. N.; Engelhard, M. H.; Luo, J.; Yin, J.; Chen, Y.; Zhong, C. J. *J. Am. Chem. Soc.* **2012**, *134*, 15048−15060.
40. Wu, J.; Shan, S.; Petkov, V.; Prasai, B.; Cronk, H.; Joseph, P.; Luo, J.; Zhong, C. J. *ACS Catal.* **2015**, *5*, 5317–5327.
41. Xia, M. R.; Ding, W.; Xiong, K.; Li, L.; Qi, X. Q.; Chen, S. G.; Hu, B. S.; Wei, Z. D. *J.*

Phys. Chem. C. **2013,** *117*, 10581–10588.

42. Zhang, S.; Guo, S.; Zhu, H.; Su, D.; Sun S. *J. Am. Chem. Soc.* **2012**, *134*, 5060−5063.
43. Petkov, V.; Shan, S.; Chupas, P.; Yin, J.; Yang, L.; Luo, J.; Zhong C. J. *Nanoscale*, **2013**, *5*, 7379–7387.
44. Fang, B.; Luo, J.; Njoki, P. N.; Loukrakpam, R.; Mott, D.; Wanjala, B.; Hu, X.; Zhong, C. J. *Electrochem. Commun.* **2009**, *11*, 1139–1141.
45. Herrero, E.; Chrzanowski, W.; Wieckowski, A. *J. Phys. Chem.* **1995**, *99*, 10423−10424.
46. Rousseau, S.; Marie, O.; Bazin, P.; Daturi, M.; Verdier, S.; Harle, V. *J. Am. Chem. Soc.* **2010**, *132*, 10832−10841.
47. Lu, A.; Peng, D.-L.; Chang, F.; Skeete, Z.; Shan, S.; Sharma, A.; Luo, J.; Zhong C. J. *ACS Appl. Mater. Interfaces* **2016**, *8*, 20082−20091.
48. Lu, A.; Chen , Y.; Li, H.; Dowd, A.; Cortie, M. B.; Xie, Q.; Guo, H.; Qi, Q.; Peng D.-L. *Int. J. hydrogen energy* **2014**, *39*, 18919−18928.
49. Caffio, M.; Cortigiani, B; Rovida, G; Atrei, A; Giovanardi, C. *J. Phys. Chem. B* **2004**, *108*, 9919−9926.
50. Shen, Y.; Xiao, K.; Xi, J.; Qiu X. *J.Power Sources* **2015**, *278*, 235−244.
51. Luo, Y.; Habrioux, A.; Calvillo, L.; Granozzi, G.; Alonso-Vante N. *Chem. Phys. Chem.* **2014**, *15*, 2136−2144.
52. Walton, A. S.; Fester, J. Bajdich, M.; Arman, M. A.; Osiecki, J.; Knudsen, J.; Vojvodic, A.; Lauritsen, J. V.; *ACS nano* **2015**, 9, 2445–2453.
53. Heimann, P.; van der Veen, J. F.; Eastman, D. E. *Solid State Commun.* **1981**, *38*, 595– 598.
54. Wanjala, B. N.; Luo, J.; Fang, B.; Mott, D.; Zhong C. J. *J. Mater. Chem.* **2011**, *21*, 4012–4020.
55. Loukrakpam, R.; Luo, J.; He, T.; Chen, Y.; Xu, Z.; Njoki, P. N.; Wanjala, B. N.; Fang, B.; Mott, D.; Yin, J.; Klar, J.; Powell, B.; Zhong C.-J. *J. Phys. Chem. C* **2011**, *115*, 1682–1694.
56. Iwasita T. *Electrochimi. Acta* **2002**, *47*, 3663–3674.
57. Neurock, M.; Janik, M.; Wieckowski A. *Faraday Discuss.* **2008**, *140*, 363–378
58. Park, K.-W.; Choi, J.-H.; Kwon, B.-K.; Lee, S.-A.; Sung Y.-E. *J. Phys. Chem. B* **2002**, *106*, 1869–1877.
59. Gordy, W.; Thomas, W. J. O. *J Chem. Phys.* **1956**, *24*, 439−444.
60. Barkholtz, H. M.; Liu D.-J. *Mater. Horiz.* **2017**, 4, 20-37.
61. Zhang, C.; Zhang, R.; Li, L.; Li, X.; Chen W. *Part. Part. Syst. Charact.* **2017**, 34, DOI: 10.1002/ppsc.201700034.
62. Fu, S.; Zhu, C.; Song, J.; Engelhard, M. H.; Xiao, B.; Du, D.; Lin Y. *Chem. Eur. J.* **2017**, 23, 10460-10464.
63. Rossouw, D.; Chinchilla, L.; Kremliakova, N.; Botton G. A. *Part. Part. Syst. Charact.* **2017**,

34, DOI: 10.1002/ppsc.201700051

64. Kang, Y.; Pyo, J. B.; Ye, X.; Gordon, T. R.; Murray C. B. *ACS nano* **2012**, *6*, 5642–5647.

65. Huang, X.; Chen, Y.; Zhu, E.; Xu, Y.; Duan, X.; Huang, Y. *J. Mater. Chem. A*, **2013**, *1*, 14449–14454.

TOC Graphic:

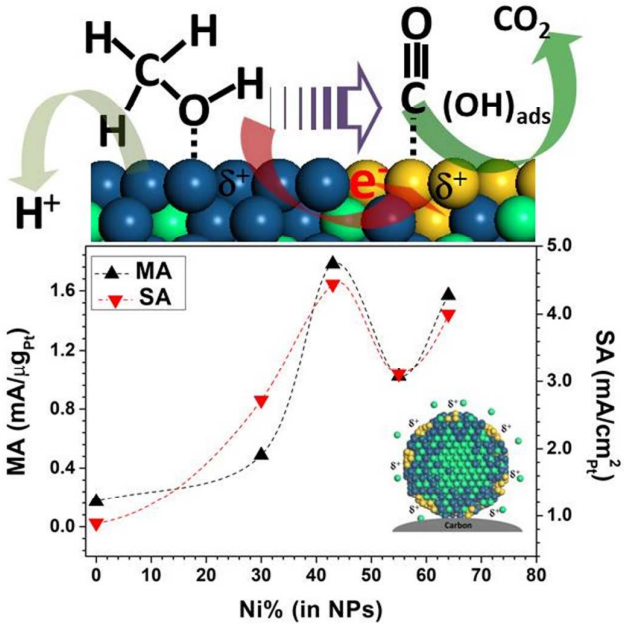
H
H
C
O
H
H
O
C
CO2
(OH)ads
H+
δ+
e-
δ+
MA
SA
MA (mA/μgPt)
SA (mA/cm2Pt)
Ni% (in NPs)
0.0
0.4
0.8
1.2
1.6
0
10
20
30
40
50
60
70
80
1.0
2.0
3.0
4.0
5.0
Carbon